ORIGINAL PAPER

T-type multilevel inverter-fed interior PM machine drives based on the voltage regulation feedback and the model predictive control

Essam E. M. Mohamed[1] · Mahmoud S. R. Saeed[1]

Abstract

The tracking of optimal current trajectories in an interior permanent magnet (IPM) synchronous machine is traditionally realized by a complex online tracking, inaccurate analytical equations, or tiresome offline calibration methods. This paper proposes a modified hybrid feed-forward/feedback flux-weakening algorithm for IPM synchronous machines. In this paper, the utilized power converter is a standard T-type multilevel inverter, and hence, the voltage and current harmonics contents of the conventional two-level inverter are improved. The control algorithm utilizes the optimal current profile for maximum torque per ampere (MTPA) operation and a voltage regulation (VR) feedback control for efficient flux-weakening operation. For infinite-speed IPM machine drives, the d-q current components are limited to follow the maximum torque per voltage (MTPV) trajectory. A low-complexity model predictive control (MPC) is employed to minimize the conflict that arises from using cascaded PI control loops for current and speed control. The performance of the drive is investigated based on the Prius 2004 IPM parameters. Extensive simulation scenarios were performed using the MATLAB/SIMULINK which validates the effectiveness of the proposed algorithm. Real-time simulations based on the dSPACE DS 1103 platform are conducted to confirm the system validity for real hardware implementation. The proposed IPM drive system proves simple structure, fast response, and low harmonic contents.

Keywords T-type · Multilevel inverter · Interior PM machine · Model predictive control · Flux-weakening control · MTPA · MTPV

Abbreviations

ω_e	Electrical angular speed
λ_{PM}	PM flux-linkage
R_s	Stator resistance
i_{dFW}	FW d-axis current component
i_{dMTPA}	MTPA d-axis current component
i_{dMTPV}	MTPV d-axis current component
i_{qFW}	FW q-axis current component
i_{qMTPA}	MTPA q-axis current component
i_{qMTPV}	MTPV q-axis current component
v_{ds}	D-axis voltage component
v_{qs}	Q-axis voltage component
Δi_{dFW}	Demagnetizing current component
I_s	Line current
I_{sMax}	Maximum line current
L_d	D-axis inductance
L_q	Q-axis inductance
EV	Electric Vehicles
FW	Flux-weakening
IPM	Interior PM
MTPA	Maximum torque per ampere
MTPV	Maximum torque per voltage
OCP	Optimal current profile
N_p	Number of pole pairs
PM	Permanent magnet
PWM	Pulse-width modulation
SVPWM	Space-vector PWM
T_d	Developed torque
T_s	Control sampling period
V_{dc}	Dc-bus voltage
VR	Voltage regulation
V_s	Supply voltage
V_{sMax}	Maximum supply voltage

✉ Essam E. M. Mohamed
   Essam.mohamed@eng.svu.edu.eg

   Mahmoud S. R. Saeed
   Mahmoud.said@eng.svu.edu.eg

[1] Department of Electrical Engineering, Faculty of Engineering, South Valley University, Qena, Egypt

1 Introduction

In the recent years, electric vehicles (EVs) received a lot of consideration as they contribute to the solution of the environmental problems in two phases. Firstly, the oil resources are limited, and hence, the enlarged use of EVs conserves oil resources for critical applications. Secondly, the use of EVs reduces the use of internal combustion engines, and hence, the oil emissions are reduced [1]. Electric motors are the muscles of EVs that convert electric energy to mechanical energy that drives the vehicle. The drive electric motor must grant improved torque and power density, extended torque-speed curve, high efficiency, and feasible cost. Induction motors are employed in the Tesla Model S to avoid the usage of expensive rare-earth magnets and to benefit from the high reliability; however, the high starting current represents a challenge for the inverter and battery design [2]. Interior permanent magnet (IPM) machines provide high efficiency and high dynamic performance. They are employed in the Nissan Leaf, Toyota Prius 2004, Camry 2007, and Lexus 2005 [3].

The two-level voltage source inverters (VSIs) are the classical form of power converters in IPM motor drives. However, nowadays, multilevel inverters attract great attention thanks to their merits such as high-power quality, reduced switching loss, low dv/dt stress, low common-mode voltages, and reduced filter size [4]. These advantages can be met by the T-type multilevel inverter [5–7], which is considered as a perfect choice for high-power medium-voltage IPM drives.

Generally, the characteristic operation of IPMs can be divided into three regions, namely the constant torque region, flux-weakening (FW) (or constant power) region, and infinite-speed region [8]. During the constant torque region, a maximum torque per ampere (MTPA) strategy is essential to improve the motor efficiency, whereas an FW and a maximum torque per volt (MTPV) technology are required in the FW and infinite-speed regions, respectively, to extend the operating speed with the same voltage constraints [9]. These schemes can be simply implemented offline by using lookup tables [10], analytical models [11], or approximated equations [12, 13] for reference currents generation. The online MTPA/FW methods can be realized by using parameters estimation [14], signal injection [15], or optimization techniques [16, 17]. The online tracking of the MTPA/FW schemes is more accurate than offline counterpart [18]. However, online MTPA/FW schemes have excessive computational processes, which increases the hardware requirements [19]. Therefore, a compromise between tracking accuracy and hardware requirements is necessary for efficient MTPA/FW control of IPMs.

Due to system and controller complexity, the performance potentials of T-type MLI-fed IPM in the FW region have not been fully exploited. The performance of a permanent magnet synchronous machines (PMSM) fed by a T-type MLI has been investigated by [20, 21], where the power losses, efficiency and dynamic response are analysed. However, this study is limited to the constant torque region, and a classical proportional-integral (PI) controller with a carrier-based PWM technique is employed. The fault-tolerant capability and the efficiency of low-voltage low-power applications are investigated in [7, 22], respectively.

The reference currents of the MTPA/FW trajectories should be tracked by using a proper control approach, which is characterized by fast tracking response, robust operation, and constraints and nonlinear controllability. Despite the existence of simple current control schemes for IPMs such as PI or hysteresis-based controllers, only model predictive control (MPC) can satisfy the required characteristics [23]. A simple and classical form of MPC is finite control set (FCS)-MPC, which is commonly used for power electronics and motor drives [24]. However, the calculation load of FCS-MPC is the main challenging for their application in IPM drives, especially when it is applied to a T-type multi-level-based drive with multiple objectives and many switching states [25]. In addition, the attached MTPA/FW calculations further increase the computational load. Focusing on power loss reduction, a low-complexity MPC scheme is applied on an improved T-type MLI topology [26], where the dc-link voltage balance is implemented by control-set vectors grouping. Although the switching frequency of FCS-MPC is naturally variable, a constant switching frequency without the need for tuning the weighting factors is presented in [27], however, it is proposed for single-phase T-type inverters. A multiport magnetic-link T-type single-phase inverter is presented in [28]. Still, the integration of MPC with T-type MLI-fed IPM is not a common solution due to the computational load.

In this paper, a T-type multilevel inverter is employed to drive an IPM motor drive. The IPM drive is set to operate in the MTPA, FW, and infinite-speed regions. The optimal current trajectories in the three operation regions are provided by a feedforward calculation based on IPM model analysis. Furthermore, the voltage constraint is considered by using a PI-based voltage feedback regulator, which assures safe and efficient operation of the IPM within the voltage limits. The proposed scheme has the potential of simple structure compared with existing FW techniques. To avoid problems of using cascaded PI controllers for the speed and current control, a simplified FCS-MPC control is employed, and hence, the limitations that arise due to using the SV-PWM is minimized. The integration of MPC with simplified MTPA/FW controller opens new research horizons for fully implemented FW schemes with low-complexity MPC techniques. The

Fig. 1 T-type MLI fed an IPM machine
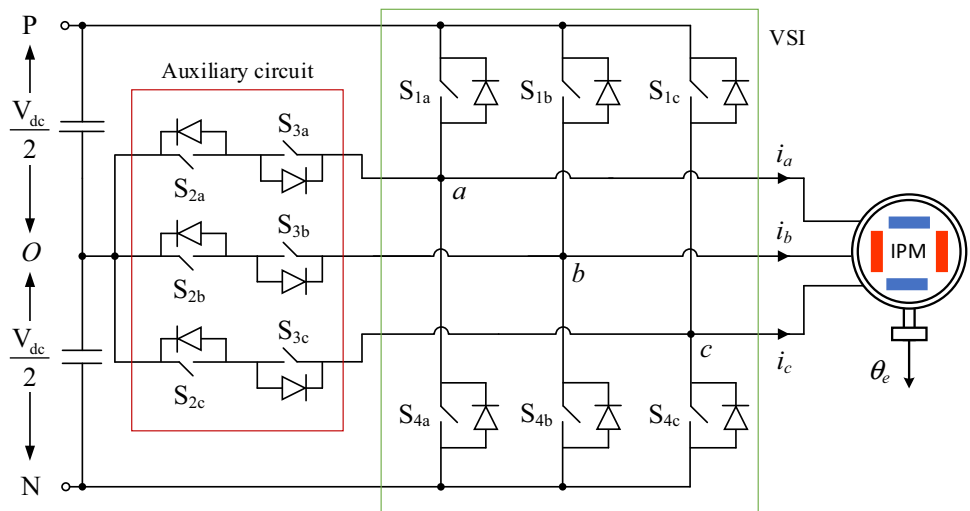
system performance is validated by extensive simulation scenarios and real-time simulations.

The paper is organized as follows: Sect. 2 presents the operation and mathematical modelling of the IPM drives fed by T-types MLI. Section 3 exhibits the proposed FW control. The simulation results are discussed in Sect. 4. The real-time simulation is exhibited in Sect. 5. Finally, the conclusions are summarized in Sect. 6.

2 The operation of the proposed drive

2.1 T-type multilevel inverter

The 3L T-type MLI is constructed by connecting two converter circuits; the first is the conventional three-phase VSI and the second is the auxiliary circuit, see Fig. 1. The VSI operates as a full-bridge two-level inverter, namely the output pole voltage $V_{\text{out}} = +V_{\text{dc}}/2$ and $V_{\text{out}} = -V_{\text{dc}}/2$. The auxiliary circuit is used to clamp the output voltage to the midpoint O; hence, the third level, $V_{\text{out}} = zero$, is introduced in the output voltage waveform. The two direction switches (S_{2x} and S_{3x}) with anti-parallel diodes are designed to enable current flow in the two directions. Table 1 presents the switching states for one phase output voltage.

For a three-phase 3L MLI, 27 states are feasible, as presented in the $\alpha - \beta$ plane in Fig. 2. The voltage vectors V_1 to V_6 represent the six large vectors of the conventional hexagon as obtained by the three-phase VSI. Vectors V_7 to V_{12} represent the medium six vectors. Vectors V_{13} to V_{18} represent six small vectors with twelve redundant switching states, six of them are positive vectors (P-type) and the other six states are negative (N-type). Finally, three zero vectors (Z_1, Z_2, and Z_3) are located in the origin. The 27 vectors with switching states can be classified as shown in Table 2.
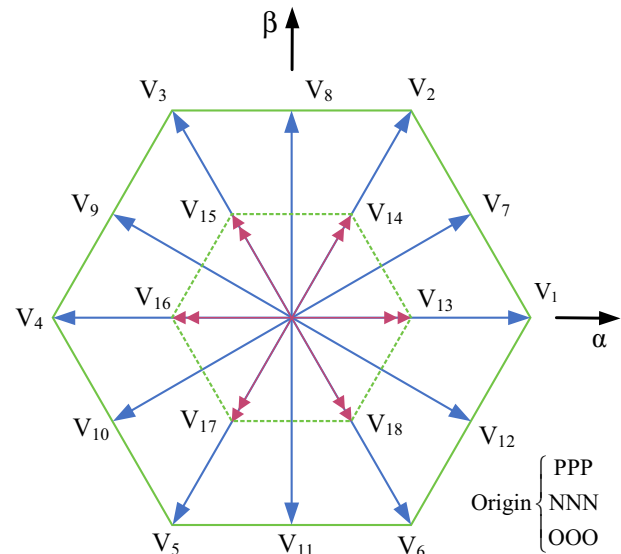

Fig. 2 Possible switching vectors in the $\alpha - \beta$ plane

2.2 IPM machine operation

The mathematical model of the IPM machine in the synchronous reference frame can be expressed as:

$$v_{\text{ds}} = R_s i_{\text{ds}} - \omega_e L_q i_{\text{qs}} + L_d \frac{di_{\text{ds}}}{dt} \tag{1}$$

$$v_{\text{qs}} = R_s i_{\text{qs}} + \omega_e (L_d i_{\text{ds}} + \lambda_{\text{PM}}) + L_q \frac{di_{\text{qs}}}{dt} \tag{2}$$

$$T_d = \frac{3}{2} N_P [\lambda_{\text{PM}} i_{\text{qs}} + (L_d - L_q) i_{\text{qs}} i_{\text{ds}}] \tag{3}$$

where v_{ds} and v_{qs} are the stator d- and q-axis voltages, respectively. i_{ds} and i_{qs} are the stator d- and q-axis currents,

Table 1 Possible switching states for one phase ($x = a$, b, or c)

State	V_{out}	S_{1x}	S_{2x}	S_{3x}	S_{4x}
P	$+V_{\text{dc}}/2$	ON	OFF	OFF	OFF
0	0	OFF	ON	OFF	OFF
0	0	OFF	OFF	ON	OFF
N	$-V_{\text{dc}}/2$	OFF	OFF	OFF	ON

Table 2 Classification of switching vectors [29]

LARGE VECTORS		MEDIUM VECTORS		SMALL VECTORS			ZERO VECTORS	
					P-TYPE	N-TYPE		
V_1	PNN	V_7	PON	V_{13}	POO	ONN	Z_1	PPP
V_2	PPN	V_8	OPN	V_{14}	PPO	OON	Z_2	NNN
V_3	NPN	V_9	NPO	V_{15}	OPO	NON	Z_3	OOO
V_4	NPP	V_{10}	NOP	V_{16}	OPP	NOO		
V_5	NNP	V_{11}	ONP	V_{17}	OOP	NNO		
V_6	PNP	V_{12}	PNO	V_{18}	POP	ONO		

respectively. R_s, ω_e, L_q, L_d, and λ_{PM} are the stator resistance, the electrical angular speed, q-axis inductance, d-axis inductance, and the PM flux-linkage, respectively. T_d and N_P are the developed torque and the number of pole pairs, respectively.

To ensure the optimal utilization of the inverter and machine, the current and voltage constraints in (4) and (5) must be fulfilled.

$$I_{\text{s}} = \sqrt{i_{\text{sd}}^2 + i_{\text{sq}}^2} \leq I_{\text{sMax}} \tag{4}$$

$$V_{\text{s}} = \sqrt{v_{\text{sd}}^2 + v_{\text{sq}}^2} \leq V_{\text{sMax}} \tag{5}$$

where I_{sMax} is the maximum line current. V_{sMax} is the maximum supply voltage based on the dc-bus voltage, V_{dc}, and the applied modulation strategy as can be calculated by (6).

$$V_{\text{sMax}} = \begin{cases} \frac{1}{2} V_{\text{dc}}, & sine - PWM \\ \frac{1}{\sqrt{3}} V_{\text{dc}}, & space - vector\,PWM \\ \frac{2}{\pi} V_{\text{dc}}, & six - step\,operation \end{cases} \tag{6}$$

The current and voltage limits imposed by (4) and (5) force the drive to operate within a predefined profile for optimal efficiency and dynamic operation of the IPM drive. As can be seen from Fig. 3, the MTPA operation is accomplished when the drive current follows the oA trajectory, where the operating point is defined by the intersection point with the torque hyperbola. Point A defines the rated voltage, current, torque, and speed of the drive. When the drive speed exceeds the rated speed, the current vector moves on the AB trajectory. The current vector preserves the maximum current

value, while the d-axis current is employed to weaken the flux-linkage, i.e. the drive operates in the flux-weakening region. To preserve the maximum limit of current, the q-axis component is decreased along with the developed torque. For IPM machines, it is possible to design the characteristic current point, $C = \frac{\lambda_{\text{PM}}}{L_{\text{d}}}$, inside the current limit circle, then the MTPV region exists, and the drive can theoretically operate at infinite speed. This mode of operation is defined by a current vector moves on the BC trajectory, i.e. decreasing both the d-q axis current components. This leads to less flux-linkage weakening and extra torque reduction.

Based on this analysis the control algorithm is defined as follows:

- For rotor speed below the rated speed, the current vector is adjusted as (7) and (8).

$$i_{\text{dMTPA}} = \frac{\lambda_{\text{PM}}}{2(L_{\text{q}} - L_{\text{d}})} - \sqrt{\frac{\lambda_{\text{PM}}^2}{4(L_{\text{q}} - L_{\text{d}})^2} + \left(i_{\text{q}}^*\right)^2} \tag{7}$$

$$i_{qMTPA} = i_{\text{q}}^* = k_p \left(\omega_m^* - \omega_m\right) + k_i \int_0^{T_{\text{s}}} \left(\omega_m^* - \omega_m\right) dt$$

$$\leq \sqrt{I_{\text{sMax}}^2 - i_{\text{dMTPA}}^2} \tag{8}$$

This guarantees the current vector moves on the oA trajectory.

Fig. 3 IPM drive operating trajectories in the $i_d - i_q$ frame

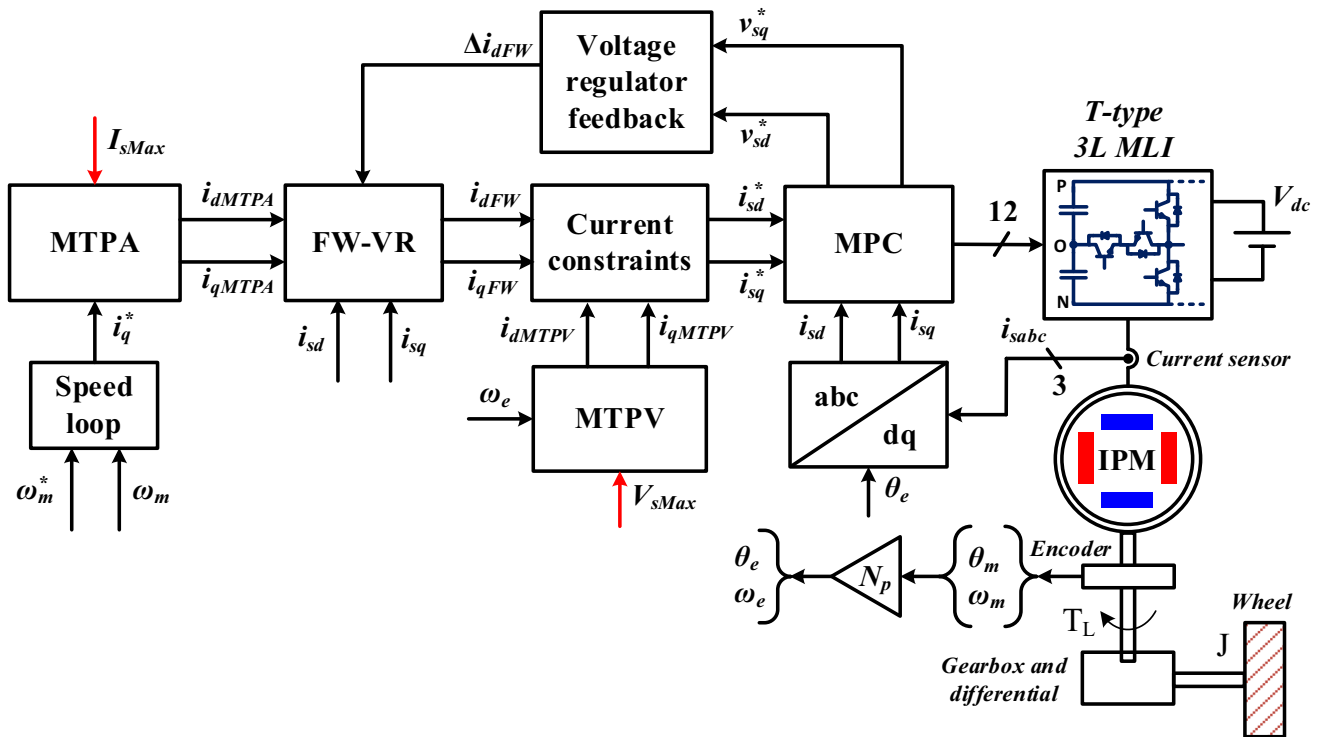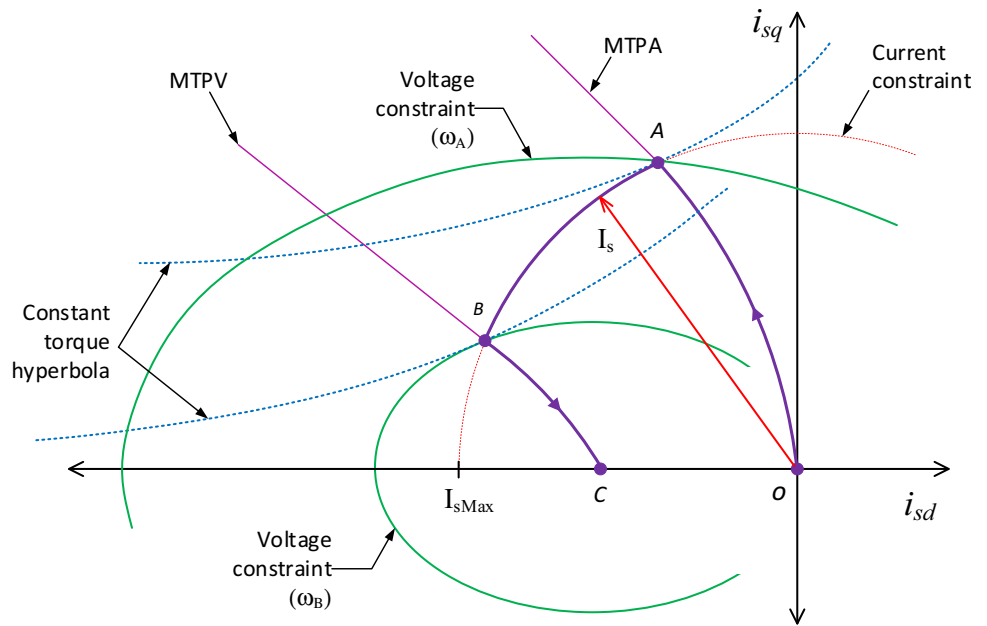**Fig. 4** Proposed FW control and the T-type MLI

- For a rotor speed beyond the rated speed, the current vector is adjusted as (9) and (10).

$$i_{\text{dFW}} = I_{\text{dMAX}} = \frac{1}{\left(L_q^2 - L_d^2\right)}\left[(L_d\lambda_{\text{PM}}) - (L_q \cdot v)\right] \quad (9)$$

$$i_{\text{qFW}} = I_{\text{qMAX}} = \sqrt{I_{\text{sMax}}^2 - i_{\text{dFW}}^2} \quad (10)$$

where, $v = \sqrt{\lambda_{\text{PM}}^2 + \left(L_q^2 - L_d^2\right)\left(I_{\text{sMax}}^2 - \dfrac{V_{\text{sMax}}^2}{\omega_e^2 L_q^2}\right)}$

- Finally, the MTPV operation is activated to allow infinite rotor speed operation, while the voltage constraint (5) is dominant. The current vector is calculated by (11) and

Fig. 5 MPC implementation on the T-type 3L MLI
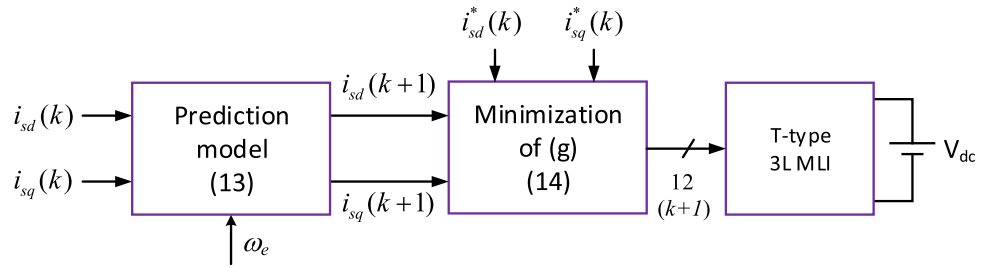
Fig. 6 Voltage regulation feedback control—d-axis current
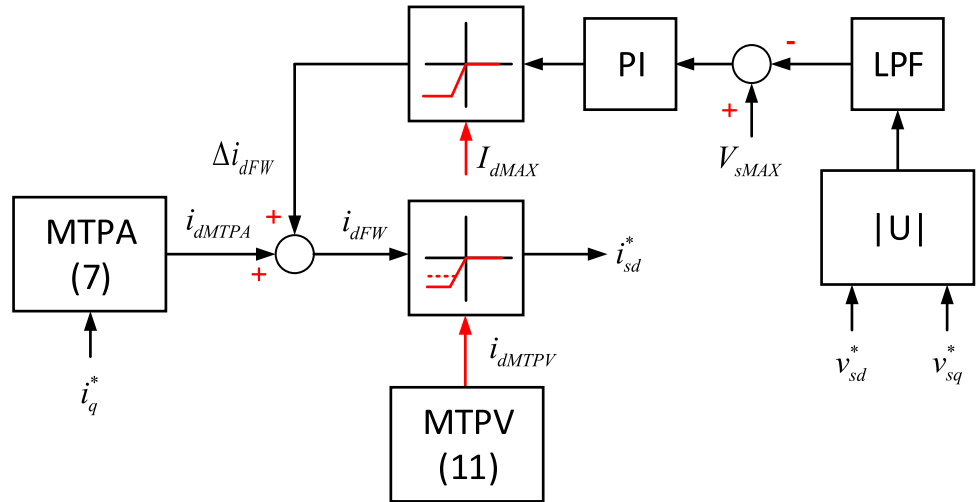
Fig. 7 Voltage regulation feedback control—q-axis current
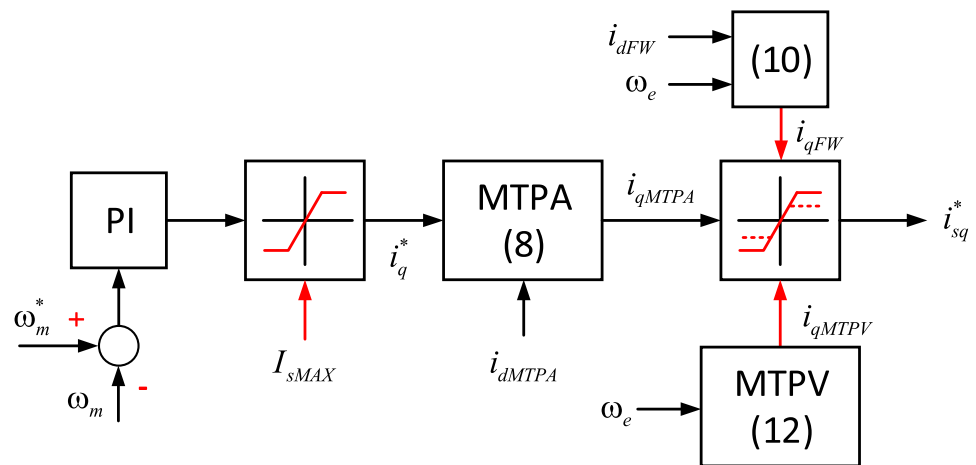
(12), i.e. it is forced to follow the *BC* trajectory.

$$i_{dMTPV} = \frac{1}{L_{\mathrm{d}}} \left(\frac{1}{4(L_{\mathrm{q}} - L_{\mathrm{d}})} \left(L_{\mathrm{q}}\lambda_{\mathrm{PM}} - \zeta \right) \right) \tag{11}$$

$$i_{qMTPV} = \frac{1}{L_{\mathrm{q}}} \left(\sqrt{\left(\frac{V_{\mathrm{sMax}}}{\omega_{\mathrm{e}}} \right)^2 - \lambda_{\mathrm{PM}}^2} \right) \tag{12}$$

where $\zeta = \sqrt{(L_{\mathrm{q}}\lambda_{\mathrm{PM}})^2 + 8(L_{\mathrm{q}} - L_{\mathrm{d}})^2 \left(\frac{V_{\mathrm{sMax}}}{\omega_{\mathrm{e}}} \right)^2}$

3 Proposed FW control

The proposed algorithm is shown in Fig. 4. A three-level (3L) T-type MLI is used instead of the three-phase VSI. Due to the complex design of classical PI controller with 3L SVPWM, an FCS-MPC is utilized to implement the current control loop for fast tracking of optimal current trajectories. The voltage regulation feedback control is used to adjust the d-axis current component according to the operating region.
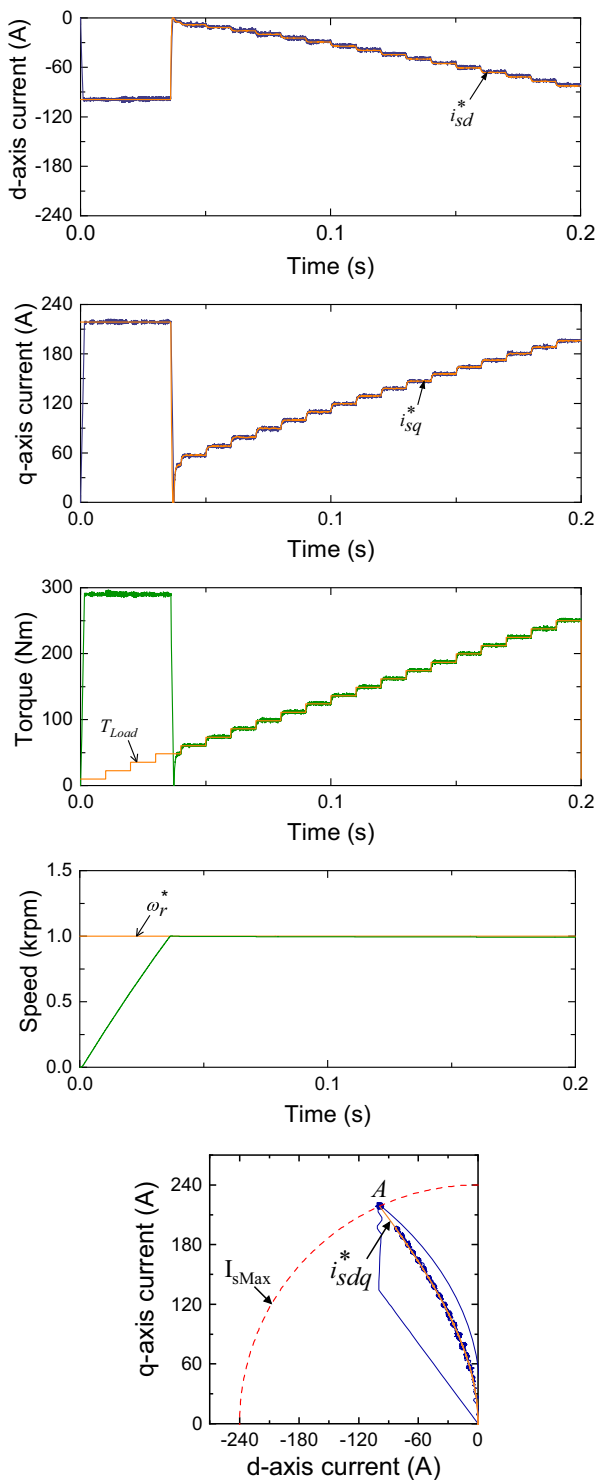
Fig. 8 Simulation performance of MTPA-MPC

Fig. 9 Simulation performance of MTPA-SVPWM

3.1 Model predictive control

MPC is applied as a current control scheme to avoid the limitations of the conventional linear controllers. For example, classical PI controllers have some limitations such as the
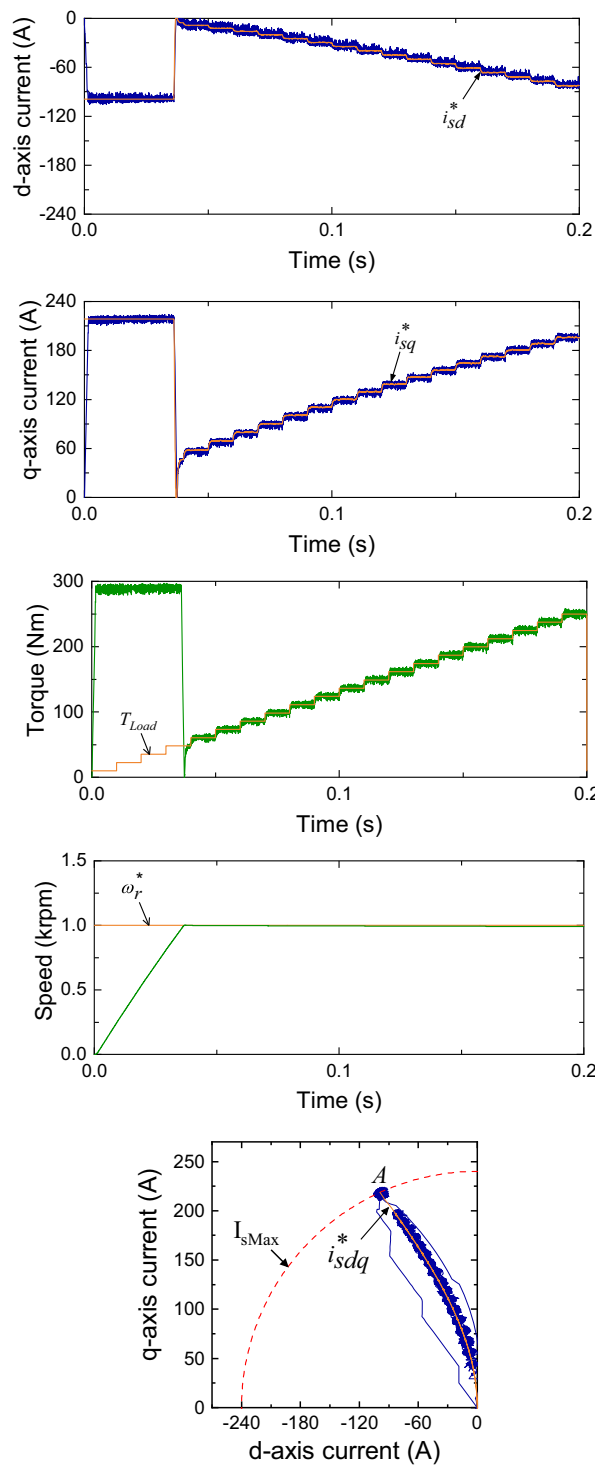
windup, overshoot, and complex parameters' tunning and pulse generation. On the other hand, the FCS-MPC strategy utilizes the discrete nature of DSP and microcontrollers to apply an optimal switching state in a very intuitive concept. Hence, measurements of the current period are used to calculate the optimal control vector that provide fast tracking of the d-q axis currents and speed demands.

Fig. 10 Line current FFT and
THD analysis

a) MTPA-MPC

b) MTPA-SVPWM
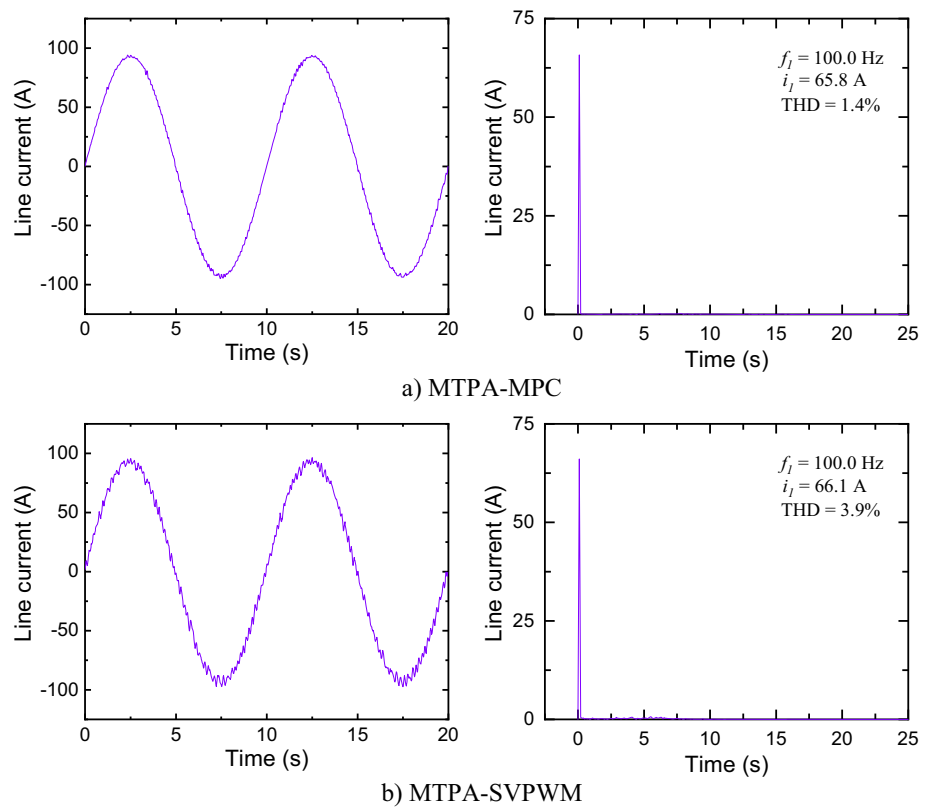
Table 3 Simulation parameters [39, 40]

d-axis inductance, L_d	1.6 (mH)
Magnet flux linkage, λ_{PM}	175.7 (mWeb)
Maximum inverter current	240 (A)
Moment of inertia, J	0.089
Number poles pairs, N_P	4
q-axis inductance, L_q	2.1 (mH)
Rated speed	1500 (rpm)
PI-SVPWM switching frequency	5 (kHz)
Control sampling period, T_s	2×10^{-5} (s)
Model sampling interval, T_{ss}	2×10^{-5} (s)
Speed controller	$k_p = 20, k_i = 1.5$
Voltage feedback regulator	$k_p = 0.5, k_i = 10 \times 10^{-6}$
Stator resistance, R_s	6.5 (mΩ)
Supply voltage, V_{dc}	500 (V)

The implementation process can be summarised as shown in Fig. 5. First, the continuous-time model of the IPM machine, in (1) and (2), is discretized using the first-order Euler discretization. Second, the measured d-q axis currents at the current sample (k) are used to predict the d-q axis currents for the next sample $(k + 1)$, as given in (13) [30–32]. Third, the optimal voltage vector is selected based on the minimization of the cost function as given in (14). Finally,

the switching signals based on the optimal voltage vector are applied to the 3L MLI. It should be noticed that the control set of the proposed FCS-MPC scheme is divided into two groups based on the voltages effect on the neutral point voltage. Therefore, the neutral point voltage is explicitly regulated without including a balancing function in the objective function, and the weighting factor is removed. Furthermore, the number of enumerated vectors is reduced. Thus, the proposed MPC technique is simplified, and it can be easily integrated with the proposed FW strategy.

$$
\left.
\begin{aligned}
i_{sd}(k+1) &= \left(1 - \frac{R_s}{L_d} T_s\right) i_{sd}(k) \\
&+ \left(\frac{L_q}{L_d}\right) T_s i_{sq}(k) \omega_e(k) \\
&+ \left(\frac{T_s}{L_d}\right) u_{sd}(k) \\
i_{sq}(k+1) &= \left(1 - \frac{R_s}{L_q} T_s\right) i_{sq}(k) \\
&- \left(\frac{L_d}{L_q} i_{sd}(k) + \frac{\lambda_{PM}}{L_q}\right) T_s \omega_e(k) \\
&+ \left(\frac{T_s}{L_q}\right) u_{sq}(k)
\end{aligned}
\right\}
\tag{13}
$$

$$
g = (i_{sd}^* - i_{sd}(k+1))^2 + (i_{sq}^* - i_{sq}(k+1))^2
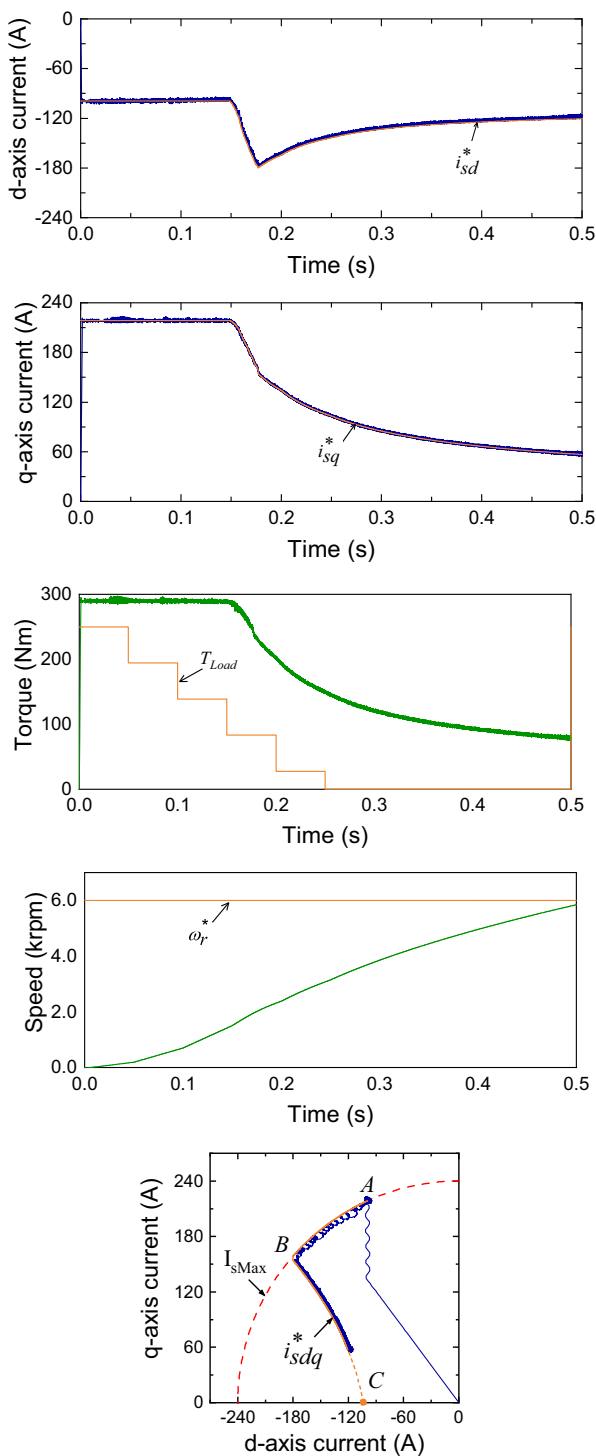\tag{14}
$$
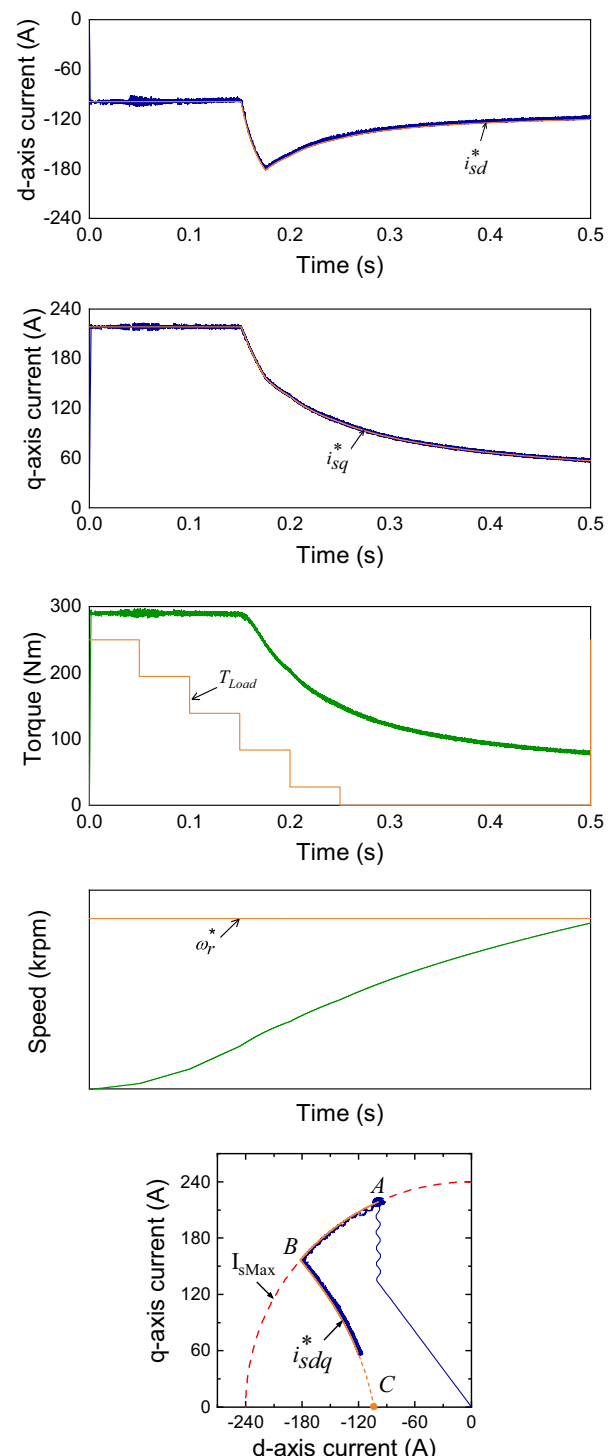
Fig. 11 Simulation performance of MPC-VR

Fig. 12 Simulation performance of MPC-OCP

3.2 Voltage regulation feedback control

The FW control is implemented using the voltage regulation (VR) feedback control [3, 33–35].

The voltage regulation feedback control adjusts the d-axis current based on the shortage between the reference volt-

age vector (v_{sd}^* and v_{sq}^*) and the maximum inverter voltage V_{sMax}. As shown in Fig. 6, the amplitude of the voltage reference voltage is calculated and filtered out using a LPF, and then, it is compared with V_{sMax}. The LPF plays two rules; first, it guarantees more stable operation by rejecting the steady-state noise in the voltage feedback loop [36, 37].

In addition, smooth transient is presented by limiting the controller response to the low-frequency component [38].

When the reference voltage vector is higher than V_{sMax}, the voltage regulation feedback loop is activated, and the PI controller modifies the d-axis current to follow the FW path (AB) in Fig. 3. The demagnetizing component is calculated as,

$$i_{dFW} = i_{dMTPA} + \Delta i_{dFW} \tag{15}$$

The minimum and maximum limits of i_{dFW} are set to zero and I_{dMAX}, where I_{dMAX} is calculated by (16).

$$I_{dMAX} = -I_{sMax} - i_{d(A)} \tag{16}$$

where $i_{d(A)}$ is the d-axis component of point (A) in Fig. 3 [34].

For the infinite speed IPM machine drives, the MTPV is activated to adjust the d-axis current reference to follow the (BC) trajectory. This is accomplished by limiting i_{dFW} according to the value of i_{dMTPV}.

The q-axis component reference is calculated based on the speed controller demand. As shown in Fig. 7, the MTPA is employed to calculate i_{qMTPA} based on (8). Two limits are applied to i_{qMTPA}, the first guarantees that the current reference fulfils the drive's current limit by limiting i_{qMTPA} with i_{qFW}, as calculated by (9). The second limit is activated only when the machine operates on the MTPV trajectory. Hence, i_{qMTPV}, as calculated by (12), is applied to limit i_{qMTPA} to the final value of i_{sq}^*.
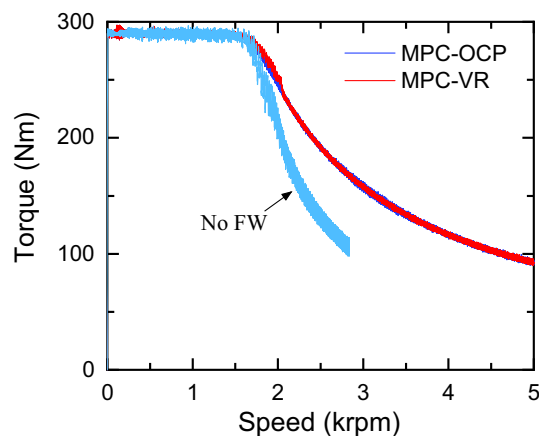
It can be seen from Fig. 6 that the VR feedback control operates without the need for machine parameters, and hence, the effect of temperature and/or parameters uncertainty is avoided during the FW region.

4 Simulation results

A MATLAB Simulink model was built to study the performance of the proposed drive as shown in Fig. 4. The IPM, MLI, and controllers' parameters are given in Table 3. In order to study a realistic system, Prius IPM motor parameters are used in the simulation of this paper [39, 40].

4.1 MTPA operation

To study the performance of the MTPA operation, the simulation model has been designed to follow the OA trajectory, i.e. the FW algorithm is not activated. Hence, in this region, the performance of the MLI with two different control techniques, namely the MTPA along with the MPC (MTPA-


a) Torque-speed curve
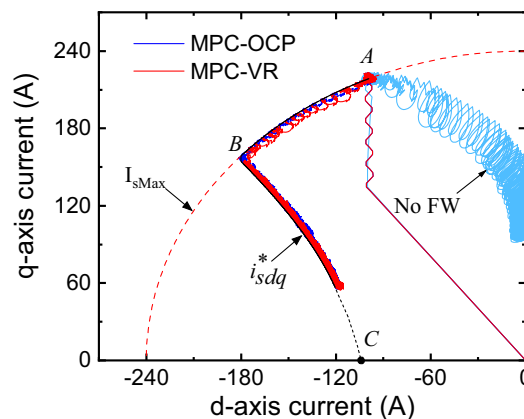
b) q-axis vs. d-axis currents

Fig. 13 Performance comparison

MPC) and the MTPA along with the SVPWM (MTPA-SV). A reference speed of $\omega_r^* = 1.0$krpm is applied to the speed controller, while the load torque is changed from 0 to 250 Nm. This ensures the drive operation below the FW region; meanwhile, the reference current vector moves on the OA trajectory.

Comparing the two control techniques, as shown in Figs. 8 and 9, shows similar dynamic performance, i.e. the two scenarios fulfil the speed control commands, and the line and d-q axis currents track the reference current commands. However, the torque ripples in the MTPA-MPC technique are lower than that in the MTPA-SV technique due to the decreased ripples of the d-q current components, while the optimal current vector is applied. Also, the sampling interval of the proposed MPC is small enough to accurately track the optimal current vector. This can be confirmed by comparing the FFT analysis of the line current as given in Fig. 10. This FFT analysis has been done at steady-state operation with a load torque of 100 Nm and a rotor speed of 1.5krpm. The FFT analysis shows reduced harmonics content of the MTPA-MPC technique with a THD of 1.4%. The MTPA-SV algorithm exhibits a higher THD of 3.9%.

Fig. 14 Set-up for the real-time simulation
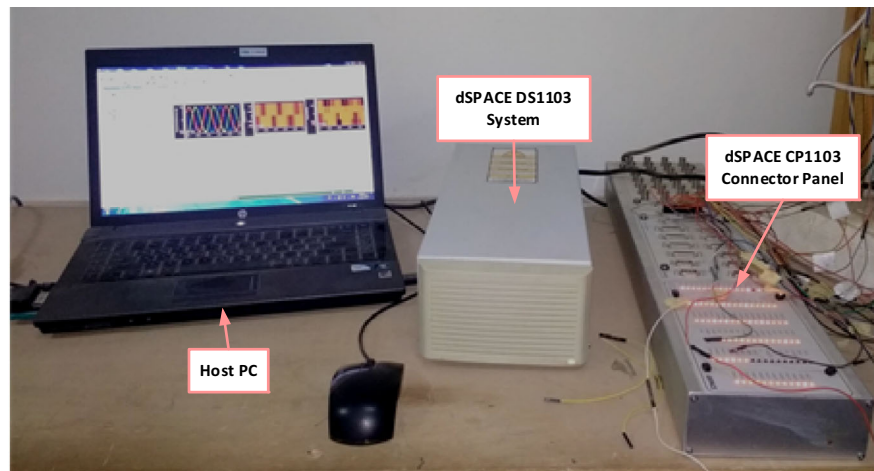
4.2 FW and MTPV operation

When the system operates in the FW and MTPV regions, the performance of two algorithms can be compared, namely the MPC along with the VR control (MPC-VR) and the MPC along with the optimal current profile (OCP) control (MPC-OCP).

The simulation model is prepared to force the drive operation in both the FW and the MTPV regions by following the ABC trajectory. Hence, the reference speed is set to a high value of 6.0 krpm, to ensure the drive operation in the FW region. The load torque is decreased in steps from 250 Nm at starting to zero at 0.25 s, and hence, the current vector is forced to move on the ABC trajectory. Beyond the instant 0.25 s, the load torque is kept at zero to allow maximum acceleration of the motor, and high-speed operation is obtained.

It can be seen, from Figs. 11 and 12, that the proposed MPC-VR algorithm successfully controls the MLI in both the FW and the MTPV regions. The d-q axis current components track the d-q reference components in the FW and MTPV regions and hence the torque-speed curve has been extended compared to the drive operation while the VR algorithm is not applied, see Fig. 13. Also, the MPC-VR provides the same performance as the conventional OCP control (MPC-OCP), and however, cascaded PI speed and current controllers are avoided. Besides, system parameters are necessary to implement the OCP control, and hence, the system performance in practical application is affected by temperature and system parameters uncertainty.

5 Real-time simulation

The complexity of MLI and IPM machine drives imposes fast, safe, and cost-effective design and testing solutions. Recently, real-time (RT) simulations deliver all these features. In addition, system operation with the designated DSPs is confirmed where the RT simulation is performed at the actual operating frequency [41]. The dSPACE DS1103 system is used to test the operation of the T-type MLI and the IPM machine drive. First, the SIMULINK model is prepared for RT simulation [42]. The dSPACE ControlDesk interface, which is shown in Appendix, is employed to process the model, run the RT simulation, and store the results. Second, the SIMULINK model is uploaded to the dSPACE ControlDesk, where the C code for the model is generated. Third, the C code is uploaded to the dSPACE DS1103 board where it is being tested for RT operation. The dSPACE DS1103, the host PC, and the dSPACE CP1103 connection panel are shown in Fig. 14. The host PC has the MATLAB/SIMULINK and the dSPACE ControlDesk installed. The real-time simulation results are shown in Fig. 15 for a fixed load torque of 50 Nm at 1500 rpm, 2000 rpm, 2500 rpm, and 3000 rpm rotor speeds. For the 1500 rpm case, the drive operates at rated speed and the d-q axis current components are calculated accordingly by the MTPA algorithm, while the waveforms show sinusoidal line currents. The 3L operation of line voltage is verified by the phase and line voltage waveforms. The torque and speed fulfil the load and controller demands. The same performance is obtained for the 2000 rpm, 2500 rpm, and 3000 rpm cases, while the d-q axis current components are adapted based on the FW and the MTPV algorithms.

6 Conclusion

This paper investigates the operation of the T-type MLI-fed IPM machine drive. The VR feedback FW algorithm and the MPC are employed to control the drive in the FW region. The drive operation is compared with the conventional OCP FW control, while the T-type MLI is driven by the SVPWM. The employed MPC scheme utilizes the redundant voltage vectors to balance the dc-link voltage; hence, no weighting factor is required, and reduced enumeration process is implemented. The integration of the proposed FW control with a low-complexity FCS-MPC algorithm has provided several
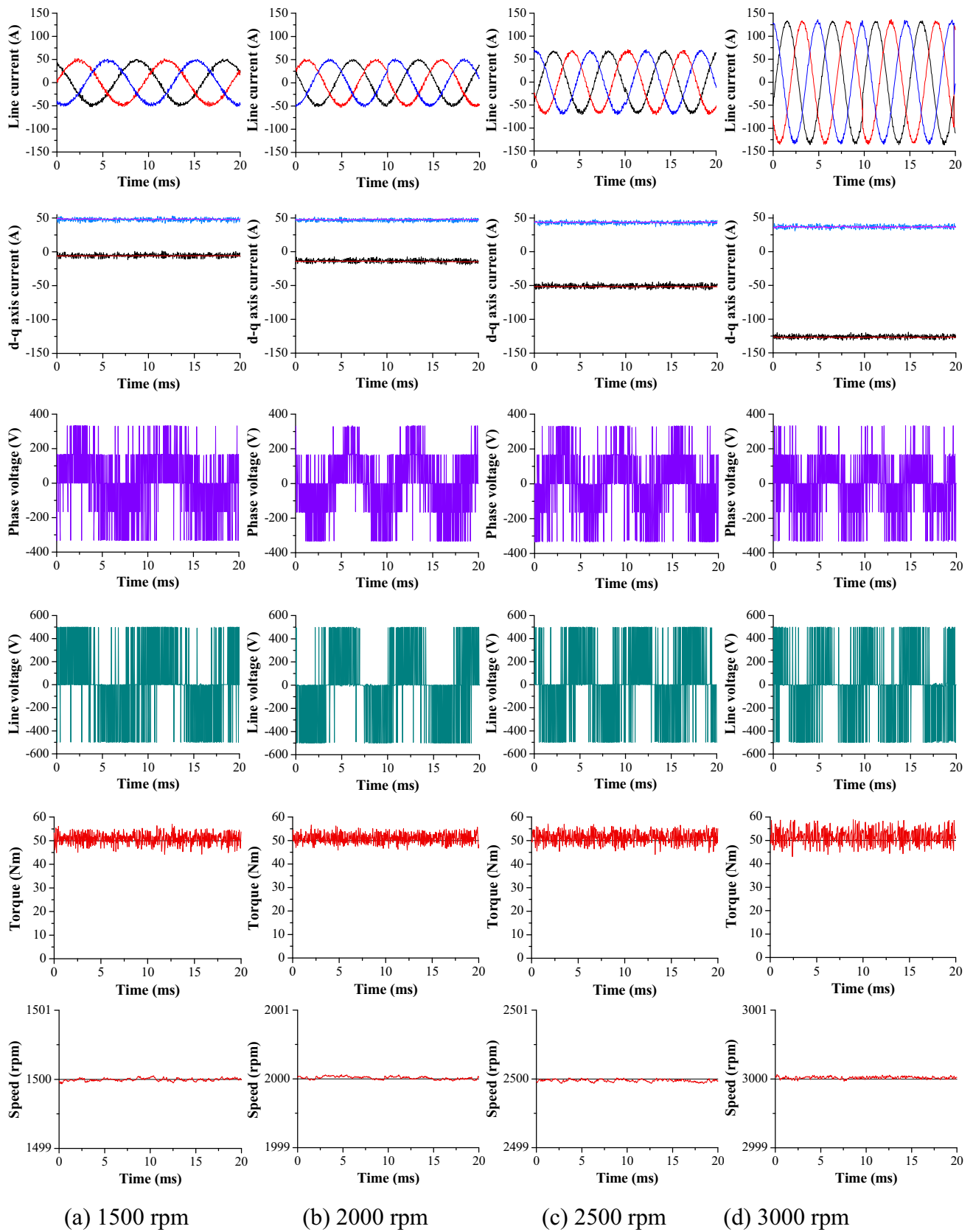
(a) 1500 rpm   (b) 2000 rpm   (c) 2500 rpm   (d) 3000 rpm

Fig. 15 Real-time simulation results at a fixed load torque of 50 Nm

potentials of fast tracking, simple structure, and reduced harmonics thanks to using low sample interval. The proposed drive system has proven effective operation in the MTPA, FW, and MTPV regions. In the FW and MTPV regions, the VR provides the same performance as the OCP control without dependency on system parameters. The system performance has been tested using the MATLAB/SIMULINK and hardware implementation is verified by the dSPACE DS 1103 platform.

Authors' contributions EEMM has suggested the main idea, implemented simulation work, and analysed the results. MSRS has contributed to writing, editing and reviewing this manuscript.

Data availability Not applicable.

Declarations

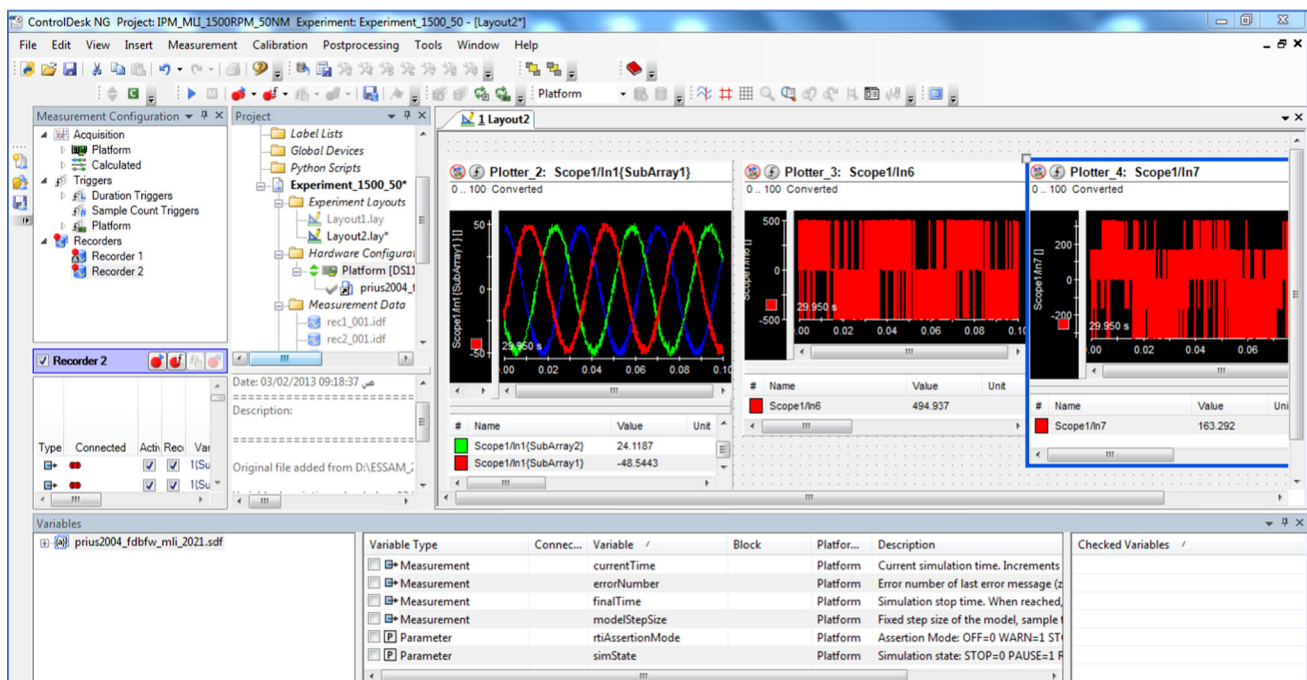**Conflict of interest** The authors declare that he has no conflicts of interest to disclose.

Ethical approval Not applicable.

Appendix

Screenshot of the dSPACE ControlDesk user interface.

References

1. Mi C, Masrur MA (2017) Hybrid Electric Vehicles: Principles and Applications with Practical Perspectives. Wiley, New York
2. Huynh TA, Hsieh M-F (2018) Performance analysis of permanent magnet motors for electric vehicles (EV) traction considering driving cycles. Energies 11(6):1385
3. Mohamed EEM (2020) Voltage regulation feedback and deadbeat predictive current control of interior PM machines. Int Trans Electr Energ Syst. https://doi.org/10.1002/2050-7038.12413
4. Rodriguez J, Jih-Sheng L, Fang-Zheng P (2002) Multilevel inverters: a survey of topologies, controls, and applications. IEEE Trans Ind Electron 49(4):724–738. https://doi.org/10.1109/TIE.2002.801052
5. Wang X, Wang Z, Wang W, Cheng M (2019) Fault diagnosis of sensors for T-type three-level inverter-fed dual three-phase permanent magnet synchronous motor drives. J. Power Electron. Drives 4(1):167–178
6. Wang Z, Wang X, Cheng M, Hu Y (2017) Comprehensive investigation on remedial operation of switch faults for dual three-phase PMSM drives fed by T-3L inverters. IEEE Trans Ind Electron 65(6):4574–4587
7. Wang X, Wang Z, Cheng M, Hu Y (2017) Remedial strategies of T-NPC three-level asymmetric six-phase PMSM drives based on SVM-DTC. IEEE Trans Ind Electron 64(9):6841–6853
8. Miguel-Espinar, C., Heredero-Peris, D., Villafafila-Robles, R., Montesinos-Miracle, D.: Review of flux-weakening algorithms to extend the speed range in electric vehicle applications with permanent magnet synchronous machines. IEEE Access (2023)
9. Tinazzi, F., Bolognani, S., Calligaro, S., Kumar, P., Petrella, R., Zigliotto, M.: Classification and review of MTPA algorithms for synchronous reluctance and interior permanent magnet motor drives. In: Proceedings of the 21st European Conference on Power Electronics and Applications. IEEE, pp. P. 1-P. 10 (2019).
10. Chen S-G, Lin F-J, Liang C-H, Liao C-H (2021) Development of FW and MTPV control for SynRM via feedforward voltage angle control. IEEE ASME Trans. Mechatron. 26(6):3254–3264
11. Varatharajan A, Pellegrino G, Armando E (2021) Direct flux vector control of synchronous motor drives: a small-signal model for optimal reference generation. IEEE Trans Power Electron 36(9):10526–10535
12. Shakib, S. S. I., Xiao, D., Dutta, R., Alam, K. S., Osman, I., Rahman, M.: An improved modulated model predictive torque and flux control for high-speed IPMSM drives. In: Proceedings IEEE Energy Conversion Congress and Exposition (ECCE). IEEE, pp. 6601–6607 (2019)
13. Xiao R, Peng S, Huang Z, Chen G (2022) Deep flux weakening control strategy for IPMSM with variable direct axis current limitations. Electr Eng 104(5):3425–3434
14. Sanz A, Oyarbide E, Gálvez R, Bernal C, Molina P, San-Vicente I (2019) Analytical maximum torque per volt control strategy of an interior permanent magnet synchronous motor with very low battery voltage. IET Electr Power Appl 13(7):1042–1050
15. Chen Z, Yan Y, Shi T, Gu X, Wang Z, Xia C (2020) An accurate virtual signal injection control for IPMSM with improved torque output and widen speed region. IEEE Trans Power Electron 36(2):1941–1953
16. Kim H-S, Lee Y, Sul S-K, Yu J, Oh J (2019) Online MTPA control of IPMSM based on robust numerical optimization technique. IEEE Trans Ind Appl 55(4):3736–3746
17. Lu, Y., He, S., Li, C., Luo, H., Yang, H., Zhao, R.: Online full-speed region control method of IPMSM drives considering cross-saturation inductances and stator resistance. IEEE Trans. Transp. (2023)
18. Huang Z, Lin C, Xing J (2020) A parameter-independent optimal field-weakening control strategy of IPMSM for electric vehicles over full speed range. IEEE Trans Power Electron 36(4):4659–4671
19. Xia Z et al (2020) Computation-efficient online optimal tracking method for permanent magnet synchronous machine drives for MTPA and flux-weakening operations. IEEE J. Emerg. Sel. Top. Power Electron. 9(5):5341–5353
20. Salem, A., Belie, F. D., Sergeant, P., Abdallh, A., Melkebeek, J.: Loss evaluation of interior permanent-magnet synchronous Machine drives using T-type multilevel converters. In: Proceedings of the IEEE 15th International Conference on Environment and Electrical Engineering (EEEIC), 10–13 June 2015, pp. 101–106 (2015). https://doi.org/10.1109/EEEIC.2015.7165465
21. Liang, D., Li, J., Qu, R., Zheng, P., Song, B.: Evaluation of high-speed permanent magnet synchronous machine drive with three-level and two-level inverter. In: Proceedings IEEE International Electric Machines and Drives Conference, 10–13 May 2015, pp. 1586–1592 (2015). https://doi.org/10.1109/IEMDC.2015.7409275
22. Shin S-M, Ahn J-H, Lee B-K (2015) Maximum efficiency operation of three-level T-type inverter for low-voltage and low-power home appliances. J. Electr. Eng. Technol. 10(2):586–594
23. Kouro S, Cortés P, Vargas R, Ammann U, Rodríguez J (2009) Model predictive control—a simple and powerful method to control power converters. IEEE Trans Ind Electron 56(6):1826–1838
24. Karamanakos P, Geyer T (2020) Guidelines for the design of finite control set model predictive controllers. IEEE Trans Power Electron 35(7):7434–7450
25. Boudja, W., Barra, K., Remache, S., Mekhilef, S., Wira, P.: Optimized T-type multilevel converter under Finite Set Model Predictive Control. In: Proceedings 2nd 2nd International Conference on Advanced Electrical Engineering (ICAEE). IEEE, pp. 1–6 (2022)
26. Yang G, Hao S, Fu C, Chen Z (2019) Model predictive direct power control based on improved T-type grid-connected inverter. J. IEEE Emerg. Sel. Top. Power Electron. 7(1):252–260
27. Yang Y, Wen H, Fan M, Xie M, Chen R, Wang Y (2019) A constant switching frequency model predictive control without weighting factors for T-type single-phase three-level inverters. IEEE Trans Ind Electron 66(7):5153–5164
28. Khan, S. A., Guo, Y., Khan, M. N. H., Siwakoti, Y., Zhu, J.: Model predictive control without weighting factors for T-type multilevel inverters with magnetic-link and series stacked AC-DC modules. In: Proceedings under IEEE Energy Conversion Congress and Exposition (ECCE).IEEE, pp. 5603–5609 (2019).
29. Salem A, Abido MA (2019) T-type multilevel converter topologies: a comprehensive review. Arab J Sci Eng 44(3):1713–1735. https://doi.org/10.1007/s13369-018-3506-6
30. Xu Y, Sun Y, Hou Y (2020) Multi-step model predictive current control of permanent-magnet synchronous motor. J Power Electron 20(1):176–187
31. Liu J, Gong C, Han Z, Yu H (2018) IPMSM model predictive control in flux-weakening operation using an improved algorithm. IEEE Trans Ind Electron 65(12):9378–9387
32. Ahmed AA (2015) Experimental implementation of model predictive control for permanent magnet synchronous motor. Int. J. Electr. Comput. Energ. Electron. Commun. Eng. 9(7):644–647
33. Kim J-M, Sul S-K (1997) Speed control of interior permanent magnet synchronous motor drive for the flux weakening operation. IEEE Trans Ind Appl 33(1):43–48
34. Li, J., et al.: Deep flux weakening control with six-step overmodulation for a segmented interior permanent magnet synchronous motor. In: Proceedings of the 20th International Conference on Electrical Machines and Systems (ICEMS). IEEE, pp. 1–6 (2017)

35. Maric, D. S., Hiti, S., Stancu, C. C., Nagashima, J. M., Rutledge, D. B.: Two flux weakening schemes for surface-mounted permanent-magnet synchronous drives. Design and transient response considerations. In: Proceedings of the IEEE International Symposium on Industrial Electronics. IEEE, vol. 2, pp. 673–678 (1999)

36. Bedetti N, Calligaro S, Petrella R (2020) Analytical design and autotuning of adaptive flux-weakening voltage regulation loop in IPMSM drives with accurate torque regulation. IEEE Trans Ind Appl 56(1):301–313

37. Jacob J, Bottesi O, Calligaro S, Petrella R (2021) Design criteria for flux-weakening control bandwidth and voltage margin in IPMSM drives considering transient conditions. IEEE Trans Ind Appl 57(5):4884–4900

38. Liu H, Zhu Z, Mohamed E, Fu Y, Qi X (2012) Flux-weakening control of nonsalient pole PMSM having large winding inductance, accounting for resistive voltage drop and inverter nonlinearities. IEEE Trans Power Electron 27(2):942–952

39. Hsu, J., Ayers, C., Coomer, C.: Report on Toyota/Prius Motor Design and Manufacturing Assessment. United States. Department of Energy, (2004)

40. Nasiri, R. A.H., Parizadeh, M., Ghayebloo, A.: A MATLAB Simulink model for Toyota Prius 2004 based on DOE reports. Presented at the The proceedings of the 14th European conference on power electronics and applications, Birmingham, UK, (2011)

41. Ensermu G, Bhattacharya A, Panigrahy N (2019) Real-time simulation of smart DC microgrid with decentralized control system under source disturbances. Arab J Sci Eng 44(8):7173–7185

42. Ghaffari, A.: dSPACE and real-time interface in Simulink. San Diego State University (2012)